Pérez, D.; Gasulla Mestre, I.; Capmany Francoy, J. (2015). Software-defined universal microwave photonics processor. Optics Express. 23(11):14640-14654. doi:10.1364/OE.23.014640.

# Software-defined reconfigurable microwave photonics processor

**Daniel Pérez,* Ivana Gasulla, and José Capmany**

*ITEAM Research Institute, Universitat Politécnica de Valencia, Camino de Vera s/n, 46022 Valencia, Spain*
** dapelo2@teleco.upv.es*

**Abstract:** We propose, for the first time to our knowledge, a software-defined reconfigurable microwave photonics signal processor architecture that can be integrated on a chip and is capable of performing all the main functionalities by suitable programming of its control signals. The basic configuration is presented and a thorough end-to-end design model derived that accounts for the performance of the overall processor taking into consideration the impact and interdependencies of both its photonic and RF parts. We demonstrate the model versatility by applying it to several relevant application examples.



**OCIS codes:** (060.2360) Fiber optics links and subsystems; (060.5625) Radio frequency photonics; (130.0250) Optoelectronics; (350.4010) Microwaves; (130.3120) Integrated optics devices.

## References and links

1. J. Capmany and D. Novak, "Microwave photonics combines two worlds," Nat. Photonics **1**, 316-330 (2007).
2. J. Yao, "Microwave photonics," J. Lightwave Technol. **27**, 314–335 (2009).
3. Technology focus on Microwave photonics, Nat. Photonics **5**, 723-736 (2011).
4. H. Al-Raweshidi and S. Komaki (Eds), *Radio over fiber technologies for mobile communications networks* (Artech House, 2002).
5. M. Sotom, B. Bénazet, A. Le Kernec, and M. Maignan, "Microwave photonic technologies for flexible satellite telecom payloads," in *Proceedings of 35th European Conference on Optical Communication*, (Vienna, Austria, 2009), pp. 1–4.
6. J. Capmany, B. Ortega, and D. Pastor, "A tutorial on microwave photonic filters," J. Lightwave Technol. **24**, 201-229 (2006).
7. M. Popov, "The convergence of wired and wireless services delivery in access and home networks," in *Optical Fiber Communication conference* (2010), paper OWQ6.
8. A. M. Koonen, M. G. Larrodé, A. Ng'oma, K. Wang, H. Yang, Y. Zheng, and E. Tangdiongga, "Perspectives of radio-over-fiber technologies," in *Optical Fiber Communication Conference* (2008), paper OThP3.
9. S. Movassaghi, M. Abolhasan, J. Lipman, D. Smith, and A. Jamalipour, "Wireless body area networks: a survey," IEEE Comms. Surv. Tut. **16**, 1658-1686 (2014).
10. See for example: http://www.pharad.com/s-q-band-rf-photonic-link.
11. D. J. Blumenthal, J. Barton, N. Beheshti, J. E. Bowers, E. Burmeister, L. A. Coldren, M. Dummer, G. Epps, A. Fang, Y. Ganjali, J. Garcia, B. Koch, V. Lal, E. Lively, J. Mack, M. Mašanović, N. McKeown, K. Nguyen, S. C. Nicholes, Hyundai Park, B. Stamenic, A. Tauke-Pedretti, H. Poulsen, and M. Sysak, "Integrated photonics for low-power packet networking," IEEE JSTQE **17**, 458-471 (2011).
12. D. A. I. Marpaung, C. Roeloffzen, R. Heideman, A. Leinse, S. Sales, and J. Capmany, "Integrated microwave photonics," Laser Photon. Rev. **7**, 506-538 (2013).
13. E. J. Norberg, R. S. Guzzon, J. S. Parker, L. A. Johansson, and L. A. Coldren, "Programmable photonic microwave filters monolithically integrated in InP–InGaAsP," J. Lightwave Technol. **29**, 1611–1619 (2011).
14. R. S. Guzzon, E. J. Norberg, J. S. Parker, L. A. Johansson, and L. A. Coldren, "Integrated InP-InGaAsP tunable coupled ring optical bandpass filters with zero insertion loss," Opt. Express **19**, 7816–7826 (2011).
15. J. S. Fandiño, J. D. Domenech, P.Muñoz, and J. Capmany, "Integrated InP frequency discriminator for phase-modulated microwave photonic links," Opt. Express **21**, 3726–3736 (2013).
16. F. Ferdous, H. Miao, D. E. Leaird, K. Srinivasan, J. Wang, L. Chen, L. T. Varghese, and A. M. Weiner, "Spectral line-by-line pulse shaping of on-chip microresonator frequency combs," Nat. Photonics **5**, 770–776 (2011).

17. M. Burla, L. R. Cort´es, M. Li, X. Wang, L. Chrostowski and J. Azaña, "On-chip ultra-wideband microwave photonic phase shifter and true time delay line based on a single phase-shifted waveguide Bragg grating," in *Proceedings of IEEE Microw. Photon. Conf.*, 2013, pp. 92–95.
18. M. Burla, D. A. I. Marpaung, L. Zhuang, C. G. H. Roeloffzen, M. R. Khan, A. Leinse, M. Hoekman, and R. G. Heideman, "On-chip CMOS compatible reconfigurable optical delay line with separate carrier tuning for microwave photonic signal processing," Opt. Express **19**, 21475–21484 (2011).
19. D. Marpaung, C. Roeloffzen, A. Leinse, and M. Hoekman, "A photonic chip based frequency discriminator for a high performance microwave photonic link," Opt. Express **18**, 27359–27370 (2010).
20. D. A. I. Marpaung, L. Chevalier, M. Burla, and C. G. H. Roeloffzen, "Impulse radio ultrawideband pulse shaper based on a programmable photonic chip frequency discriminator," Opt. Express **19**, 24838–24848 (2011).
21. D. Marpaung, "On-chip photonic-assisted instantaneous microwave frequency measurement system," IEEE Photon. Tech. Lett. **25**, 837–840 (2013).
22. Chris G. H. Roeloffzen, Leimeng Zhuang, Caterina Taddei, Arne Leinse, René G. Heideman, Paulus W. L. van Dijk, Ruud M. Oldenbeuving, David A. I. Marpaung, Maurizio Burla, and Klaus J. Boller, "Silicon nitride microwave photonic circuits," Opt. Express **21**, 22937-22961 (2013).
23. J. Mitola, "The software radio architecture," IEEE Communications Magazine **33**, 26-38 (1995).
24. P. Muñoz, J. Capmany, D. Perez, J. H. den Besten, J. S. Fandiño, and J. Domenech, "Integrated microwave photonics: state of the art and future trends," in *Proceedings of International Conference on Transparent Networks (ICTON)*, (Graz, Austria, 2014).
25. J. Capmany, J. Mora, P. Muñoz, and S. Sales, "A microwave photonics transistor," in *Proceedings of 2013 IEEE Topical meeting on MWP*, (Alexandria, USA, 2013).
26. R. Soref, "Reconfigurable Integrated optoelectronics," Advances in optoelectronics, paper 627802, (2011).
27. I. Gasulla and J. Capmany, "Analytical model and figures of merit for filtered microwave photonic links," Opt. Express **19**, 19758-19774 (2011).
28. J. S. Fandiño, J. D. Doménech, P. Muñoz, and J. Capmany, "Integrated InP frequency discriminator for phase-modulated microwave photonic links," Opt. Express **21**, 3726-3736 (2013).
29. E. J. Norberg, R. S. Guzzon, J. S. Parker, L. A. Johansson, L. A. Coldren, "Programmable photonic microwave filters monolithically integrated in InP–InGaAsP," J. Lightwave Technol. **29**, 1611-1619 (2011).
30. V. J. Urick, F. Bucholtz, P. S. Devgan, J. D. Mckinney, and K. J. Williams, "Phase modulation with interferometric detection as an alternative to intensity modulation with direct detection for analog-photonic links," IEEE Trans. Microw. Theory Tech. **55**, 978-1985 (2007).
31. China Mobile Research Institute, C-RAN: The road towards green ran. (2011, Oct.), [Online] Available: http://labs.chinamobile.com/cran/wpcontent/uploads/CRAN_white_paper_v2_5_EN.pdf.
32. Joint European Platform for photonic Integration of components and circuits (JEPPIX), The roadmap to a multibillion Euro market in integrated photonics, available at www.jeppix.eu.

## 1. Introduction

Microwave photonics (MWP), the discipline that brings together the worlds of radiofrequency (RF) engineering and optoelectronics [1-2], has attracted great interest from both the research community and the commercial sector over the past 30 years and is set to have a bright future [3]. MWP deals with the generation, processing, and distribution of microwave and millimeter-wave signals by optical means benefiting from the unique advantages inherent to photonics, such as low loss (independent of frequency), high-bandwidth and immunity to electromagnetic interference [1-2]. On top of these, MWP brings the fundamental added value of enabling the realization of key functionalities in microwave systems such as filtering, arbitrary waveform generation, frequency up/down conversion and instantaneous measurement that are either complex or even not directly possible in the radiofrequency domain. In addition, MWP creates new opportunities for information and communication (ICT) systems and networks. While initially the research activity in MWP was focused towards defense applications, it has now expanded its application areas to civil scenarios, spanning conventional areas such as cellular [4], wireless and satellite [5] communications, distributed antenna systems and optical signal processing [6], as well as emerging fields such as converged fiber-wireless [7] and in-home networks [8], medical imaging systems using terahertz (THz) waves [3], wireless body and personal area networks [9], instrumentation and the Internet of Things [3].

MWP systems are usually at the heart of analog signal processing engines that are placed in between the signal acquisition devices and front-end digital signal processors (DSPs) to accommodate the signal formats to the constraints imposed by the DSP limited sampling rates. This entails the realization of a wide variety of functionalities. Typical space, weight and power (SWAP) figures for commercial MWP systems are around 0.04-0.2 $m^2$ in size, 1.5-10 kg in weight and 15-20 W in power consumption [10], making them unsuitable for mass production and widespread use required by the next generation and emerging applications. Hence, despite the tremendous potential of MWP unveiled by the former areas, the widespread use and application of this technology is currently limited by the high cost, bulky, complex and power consuming nature of its systems. The major challenge that MWP researchers have to overcome is therefore related to reduction of SWAP figures. Solving this problem is a major challenge for the research community with expected considerable scientific, technical and economic impacts.

Integrated photonics has the potential to change the power scaling laws of high bandwidth systems through proper architectural choices that combine photonics with electronics to optimize performance, power, footprint, and cost [11]. In particular, analog photonics has a qualitatively different behavior compared to digital electronics since the energy per analog task is dominated by the steady-state bias power and does not increase significantly as the bandwidth increases [11]. Furthermore, most photonic devices are currently highly temperature dependent and therefore, temperature regulation is required, which consumes the majority of bias power. As integrated photonics favor alternative means of temperature control that draw less power, the power consumed by the photonic devices can be reduced drastically. Integrated Microwave Photonics (IMWP) [12] that aims at the incorporation of MWP components/subsystems in monolithic or hybrid photonic circuits is instrumental to achieve the aforementioned evolution objectives. The activity in IMWP has been almost exclusively focused towards the so-called Application Specific Photonic Integrated Circuits (ASPICs) where a particular circuit and chip configuration is designed to optimally perform a particular MWP functionality. ASPICs have been developed in three main technologies: Indium Phosphide (InP) [13-15], Silicon on Insulator (SOI) [16,17] and Silicon Nitride ($Si_3N_4$) for a number of applications [18-22]. As a result, there are almost as many technologies as applications and, due to this considerable fragmentation, the market for many of these application-specific technologies is too small to justify their further development into low-cost industrial mass-volume manufacturing processes.

A radically different approach that we propose in this paper is to design a software defined reconfigurable MWP signal processor architecture that can be integrated on a chip and is capable of performing all the main functionalities by suitable programming of its control signals. This is inspired, in part, by the flexibility of software-radio [23] and digital signal processors, where a common hardware is shared by multiple functionalities through a software-defined approach (or programmability), leading to significant cost reduction in the hardware fabrication. The paper is structured in the following way. Section 2 provides a top view description of the proposed processor architecture including the electrical/RF, photonic and control parts. Section 3 develops the end-to-end design equations for the electrical/RF and photonic parts of the processor while in section 4 we apply the model to several examples. A general discussion regarding the advantages, general applicability and physical insight brought by the design equations is developed in section 5. Finally in section 6 we present our conclusions.

## 2. Concept and general layout

A generic layout of the software-defined MWP signal processor architecture is illustrated in Fig. 1, where we show its operation over an arbitrary input RF signal. It comprises the RF interface and core system, the optical power source, the electrooptic (E/O) and optoelectronic (O/E) converters, the optical processing core as well as the electronics to perform the programmable control via software. The required RF, photonic and control electronic signal flows are also shown. To date, only three material platforms (shown in the right part of Fig.

1): Indium Phosphide (InP), Silicon on Insulator (SOI) either monolithic or hybrid, and Silicon Nitride ($Si_3N_4$-$SiO_2$) have reached the required degree of maturity to be considered as viable options for the implementation of complex photonic integrated circuits in general and the envisaged MWP reconfigurable processor in particular.

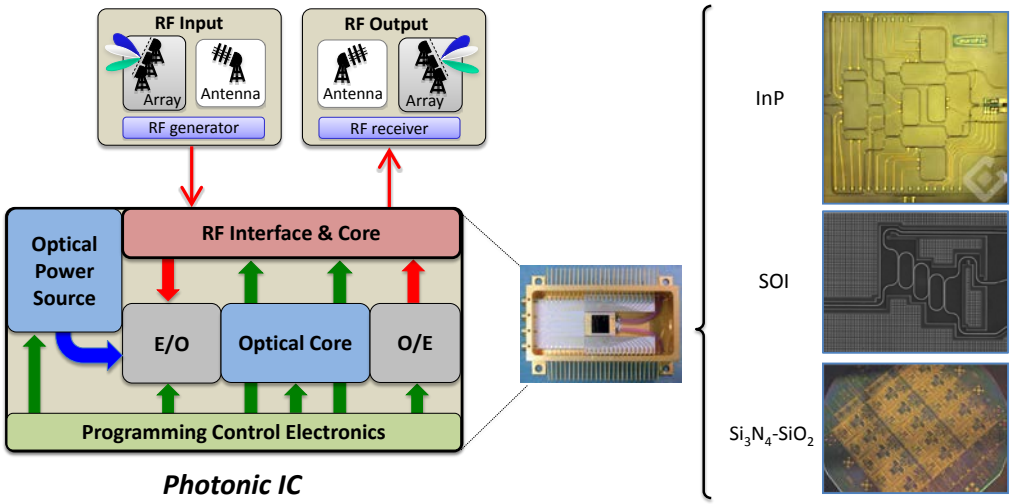


Fig. 1. Generic concept of a software-defined reconfigurable MWP signal processor and some possible material integration platforms.

The proposed software-defined reconfigurable signal processor must be capable, using the same hardware platform, of covering the main functionalities required in MWP, including: optical tunable and reconfigurable filtering, arbitrary waveform generation, optoelectronic oscillation, optically-assisted analog-to-digital conversion, frequency up- and down-conversion, instantaneous frequency measurement, frequency multiplication, tunable phase shifters and true time delay lines for optical beamforming. Some of these functionalities have been demonstrated in the above mentioned technology platforms with a variable degree of photonic component integration ranging from a modest 20% to up to a full 100% [24]. Regardless of the particular material platform employed, most of the reported ASPICs have been demonstrated for a single functionality and, to the best of our knowledge, no effort has been reported so far, towards the development of a reconfigurable software-defined MWP signal processor in a similar way as, for example, a Field Programmable Gate Array operates in electronics or a Software Radio in wireless communications, [23].

The basic skeleton of the software-defined MWP signal processor derives from the concept of the MWP transistor [25] shown in the left part of Fig. 2. The transistor is composed of different subsystems, each of which is a collection of connected fixed and variable components. We showed in [25] that this architecture is in principle capable of performing some of the required functionalities in MWP provided that its optical subsystems can be reconfigured by means of suitable control signals. Its main limitation is however that it does not support the reconfiguration of interconnections between its internal optical subsystems. This results in an intermediate performance between an ASPIC and a reconfigurable MWP processor. For example, if the reconfigurable optical filtering system in the transistor is designed as a lattice finite impulse response filter (FIR) for a MWP filtering application, then it cannot be reconfigured to implement a broadband dispersive delay line required for the generation of an arbitrary waveform (as then a grating or a photonic crystal waveguide is needed). However if both elements are present in the chip and the output from the modulator can be switched to any of them, then both functionalities can be implemented. To overcome these limitations, we propose to include programmable optical switching and routing elements into the MWP transistor architecture to provide this missing full reconfiguration flexibility. In

the same way, it is also proposed to change the reconfigurable optical filtering system by a more powerful and versatile optical core. The right layout of Fig. 2 schematizes the novel concept where optical routing and switching elements (ORSE) [26] are proposed to be included in the MWP transistor after internal modulation (represented as an E/O device), inside the optical core (not shown) and prior to detection (represented as an O/E device), to provide interconnection reconfiguration. Thus, the reconfigurable MWP signal processor requires the transformation of the basic MWP transistor architecture to accommodate, at least, three new subsystems. The first is an optical routing/switching element after modulation. This element is required to allow the use of either an internal optical source or a previously modulated or CW external source to up-convert the input RF signal. It will also allow the extraction of an auxiliary RF modulated optical signal outside the chip. Its location is shown in Fig. 2 (right) after the E/O modulator, but it may also be located before or split before and after the E/O. In principle this element should be a low-port count input/output switch or router (i.e., a 2x2 or 4x4 at most). The second ORSE subsystem is an optical routing/switching element prior to detection. Its main mission is to allow the processed up-converted RF signal either to be directly detected by the O/E or to exit the chip without being subject to optical detection. It will also allow for the injection of an optical input local oscillator to implement coherent detection of the processed up-converted RF signal. This element should be as well a low-port count input/output switch or router, although with a higher port count as compared to the input switch as it will have to enable, as well, the possibility of single and balanced direct detection. The third subsystem is a versatile optical core including different types of fixed and reconfigurable filtering elements and interconnections.

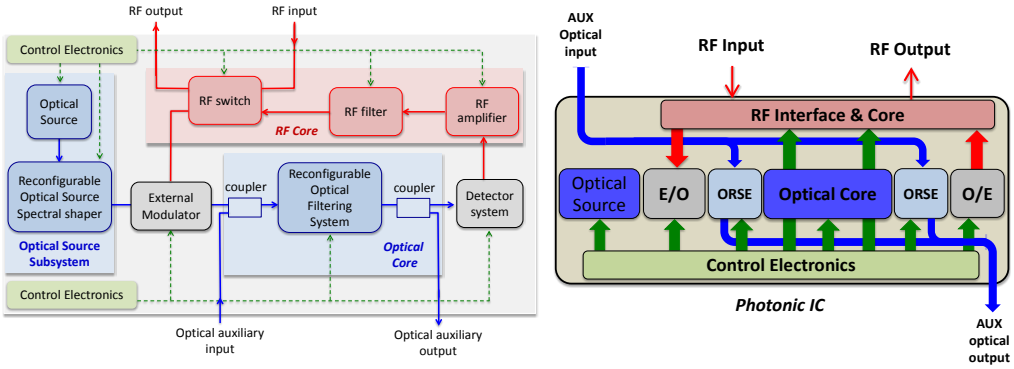


Fig. 2. Layout of (Left) a MWP transistor, from [25]; (Right) Reconfigurable MWP signal processor.

According to [25] the synthesis of any given MWP functionality can be achieved using only three different types of optical filters: FIR, infinite impulse response (IIR) and dispersive delay lines (DDL). In the most usual case, only one type is required but, in certain applications, such as arbitrary waveform generation, a cascade of two types: FIR+DDL or IIR+DDL is necessary [25]. An internal reconfigurable interconnection subsystem must be incorporated to account for all possible filter connection schemes. Again, this will require a low-port count routing/switching element.

## 3. End-to-end design model

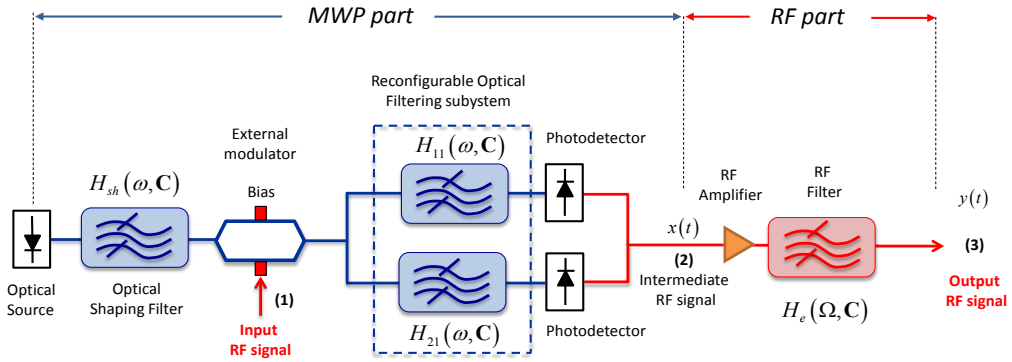


Fig. 3. Diagram of the MWP signal processor for the development of the end-to-end design model.

The design of the software-defined MWP signal processor requires a full end-to-end field-based model that provides, not only the description of the relevant linear and nonlinear signal terms, but also expressions for the evaluation of its overall figures of merit (FOMs). Figure 3 shows a basic schematic diagram of the MWP signal processor where we can easily distinguish the MWP part (comprising the above mentioned optical power source, the optical core as well as the E/O and O/E converters) from the pure radiofrequency (RF) part (composed of the RF Interface and core). The overall set of parameters that can be reconfigured by software will be identified by a vector **C**. As we can see, the MWP signal processor acts over an RF input signal (point (1) in Fig. 3) and returns an output RF signal (point (3) in Fig. 3). Within the processor, the RF input waveform is converted to the optical domain by modulating the signal produced by an optical source, which can be a fixed/tunable single wavelength laser, a comb/multiwavelength array or a broadband super-continuum source. In some cases, it may be convenient to shape the spectral characteristics of the emitter signal prior to modulation and this is done via an additional optical shaping filter that is represented by the optical transfer function $H_{sh}(\omega,\mathbf{C})$, being $\omega$ the angular optical frequency. The optical source signal is modulated by the input RF signal in an external (amplitude or phase) electrooptic modulator. After the modulator, the signal is fed to a generic reconfigurable optical filtering subsystem in order to be processed. In the case of MWP configurations where balanced detection (BD) is required, this optical subsystem can be represented as two different parallel optical filters that are characterized by the optical transfer functions $H_{11}(\omega,\mathbf{C})$ and $H_{21}(\omega,\mathbf{C})$. It must be noted that this terminology also applies to single-detection configurations simply by making $H_{11}(\omega,\mathbf{C}) = H(\omega,\mathbf{C})$ and $H_{21}(\omega,\mathbf{C}) = 0$. The output signal from the filtering subsystem is then directed towards the photodetection stage that closes the so-called MWP part of the signal processor and defines an intermediate RF signal point (point (2) in Fig. 3). From this point forward, the detected signal enters into the RF part of the signal processor where it is restored by an RF amplifier and filtered by an RF filter characterized by an electrical transfer function $H_e(\Omega,\mathbf{C})$, where $\Omega$ is the angular electrical frequency, before exiting the software-defined MWP signal processor.

In order to obtain the closed-form expressions for the overall FOMs as a function of the FOMs of both the MWP and RF parts, we will derive the linear and nonlinear RF terms in the transition point between these two segments (point (2) of Fig. 3). In our treatment and for simplicity we will not show explicitly the dependence of the transfer functions and figures of merit with the configuration vector **C** although this dependence must be understood to hold. We consider four possible operation regimes: Intensity modulation with single (*I*) or balanced (*I-BD*) detection and phase modulation with single ($\Phi$) or balanced ($\Phi$-*BD*) detection. For a modulating signal composed of two sinusoidal functions at different electrical angular frequencies $\Omega_1$ and $\Omega_2$ (point (1) of Fig. 3), the photocurrent at the output of the MWP part

considering up to the second-order and the most relevant third-order frequency contributions is given by:

$$\begin{aligned} x(t) = {} & i_1 \sin\left(\Omega_1 t + \theta_1\right) + i_2 \sin\left(\Omega_2 t + \theta_2\right) + i_{11} \sin\left(2\Omega_1 t + \theta_{11}\right) + i_{22} \sin\left(2\Omega_2 t + \theta_{22}\right) + i_{12} \sin\left[\left(\Omega_1 - \Omega_2\right) t + \theta_{12}\right] + \\ & i_{21} \sin\left[\left(\Omega_2 - \Omega_1\right) t + \theta_{21}\right] + i_{xx} \sin\left[\left(\Omega_1 + \Omega_2\right) t + \theta_{xx}\right] + i_{112} \sin\left[\left(2\Omega_1 - \Omega_2\right) t + \theta_{112}\right] + i_{221} \sin\left[\left(2\Omega_2 - \Omega_1\right) t + \theta_{221}\right], \end{aligned} \tag{1}$$

where the terms $i$ and $\theta$ refer, respectively, to the amplitude and phase of each different frequency term. Following the derivation reported in [27] for small-signal approximation, we obtain the following expressions for the amplitude of the linear and nonlinear terms in Eq. (1):

- Signal contribution, either at the angular frequency $\Omega_1$ or $\Omega_2$:

$$i_{1,2}^{Z} = \frac{I_{dc}\phi_{rf}}{2} \sin(\phi_{dc}) \left| A_{\Omega_{1,2}}^{Z} \right| \quad \text{and} \quad i_{1,2}^{Y} = 2 I_{dc}\phi_{rf} \left| A_{\Omega_{1,2}}^{Y} \right|. \tag{2}$$

- Second-order distortion, considering both the harmonic and intermodulation products:

$$\begin{aligned} & i_{112}^{Z} = \frac{I_{dc}\phi_{rf}^{2}}{8} \left| A_{2\Omega_{1,2}}^{Z} \right| \ , \ i_{12,21}^{Z} = \frac{I_{dc}\phi_{rf}^{2}}{8} \left| A_{\Omega_{1,2}-\Omega_{2,1}}^{Z} \right| \ \text{and} \ i_{xx}^{Z} = \frac{I_{dc}\phi_{rf}^{2}}{8} \left| A_{\Omega_1+\Omega_2}^{Z} \right|; \\ & i_{112}^{Y} = I_{dc}\phi_{rf}{}^{2} \left| A_{2\Omega_{1,2}}^{Y} \right| \ , \ i_{12,21}^{Y} = I_{dc}\phi_{rf}{}^{2} \left| A_{\Omega_{1,2}-\Omega_{2,1}}^{Y} \right| \ \text{and} \ i_{xx}^{Y} = I_{dc}\phi_{rf}^{2} \left| A_{\Omega_1+\Omega_2}^{Y} \right|. \end{aligned} \tag{3}$$

- Third-order distortion, considering both the harmonic and intermodulation products:

$$i_{112,221}^{Z} = \frac{I_{dc}\phi_{rf}^{3}}{32} \sin\left(\phi_{dc}\right) \left| A_{2\Omega_{1,2}-\Omega_{2,1}}^{Z} \right| \quad \text{and} \quad i_{112,221}^{Y} = \frac{I_{dc}\phi_{rf}^{3}}{2} \left| A_{2\Omega_{1,2}-\Omega_{2,1}}^{Y} \right|. \tag{4}$$

where $Z = \{I, I\text{-}BD\}$ and $Y = \{\Phi, \Phi\text{-}BD\}$ refers to one of the four possible operation regimes, $I_{dc}$ is average photocurrent defined in [27], $\phi_{rf}$ the signal modulation index and $\phi_{dc}$ the bias point for the case of intensity modulation.

The different optical spectral coefficients appearing in Eqs. (2)-(4) are defined as:

$$\begin{aligned} A_{\Omega_{1,2}}^{X} = {} & \sum_{n=\{0,1\}} \varepsilon_1 \left[ H_{11}(\omega_0 + n\Omega_{1,2}) H_{11}^{*}(\omega_0 + (n-1)\Omega_{1,2}) - H_{21}(\omega_0 + n\Omega_{1,2}) H_{21}^{*}(\omega_0 + (n-1)\Omega_{1,2}) \right] \\ & \text{for} \left\{ \varepsilon_1 = 1 \text{ if } (X = Z);\ (-1)^n \text{ if } (X = Y) \right\}; \end{aligned} \tag{5}$$

$$\begin{aligned} A_{2\Omega_{1,2}}^{X} = {} & \sum_{n=\{0,1,2\}} \varepsilon_2 \left[ H_{11}(\omega_0 + n\Omega_{1,2}) H_{11}^{*}(\omega_0 + (n-2)\Omega_{1,2}) - H_{21}(\omega_0 + n\Omega_{1,2}) H_{21}^{*}(\omega_0 + (n-2)\Omega_{1,2}) \right] \\ & \text{for} \left\{ \varepsilon_2 = \left[ (-1)^n - \cos\phi_{dc} \right] \left( \frac{1}{2} \right)^{|n-1|} \text{if } (X = Z);\ (-1)^n \left( \frac{1}{2} \right)^{|n-1|} \text{if } (X = Y) \right\}; \end{aligned} \tag{6}$$

$$\begin{aligned} A_{\Omega_{1,2}\pm\Omega_{2,1}}^{X} = {} & \pm \sum_{\substack{n=\{0,1\} \\ m=\{-1,0\}}} \varepsilon_3 \left[ H_{11}(\omega_0 + n\Omega_{1,2} \mp m\Omega_{2,1}) H_{11}^{*}(\omega_0 + (n-1)\Omega_{1,2} \mp (m+1)\Omega_{2,1}) - H_{21}(\omega_0 + n\Omega_{1,2} \mp m\Omega_{2,1}) H_{21}^{*}(\omega_0 + (n-1)\Omega_{1,2} \mp (m+1)\Omega_{2,1}) \right] \\ & \text{for} \left\{ \varepsilon_3 = \left[ (-1)^{n+m} - \cos(\phi_{dc}) \right] \text{if } (X = Z);\ (-1)^{n+m} \text{ if } (X = Y) \right\}; \end{aligned} \tag{7}$$

$$\begin{aligned} A_{2\Omega_1-\Omega_2}^{X} = {} & \sum_{\substack{n=\{0,1,2\} \\ m=\{-1,0\}}} \varepsilon_4 \left[ H_{11}(\omega_0 + n\Omega_1 + m\Omega_2) H_{11}^{*}(\omega_0 + (n-2)\Omega_1 + (m+1)\Omega_2) - H_{21}(\omega_0 + n\Omega_1 + m\Omega_2) H_{21}^{*}(\omega_0 + (n-2)\Omega_1 + (m+1)\Omega_2 \right] \\ & \text{for} \left\{ \varepsilon_4 = \left( \frac{1}{2} \right)^{|n-1|} \text{ if } (X = Z);\ (-1)^{m+n} \left( \frac{1}{2} \right)^{|n-1|} \text{ if } (X = Y) \right\}. \end{aligned} \tag{8}$$

where $X = Y$ or $Z$ represents the above-identified operation regimes and $\omega_0$ is the optical carrier angular frequency.

As reported in [27], the FOMs corresponding to the MWP part, i.e., the RF link gain $G^{X}_{MWP}$, the noise figure $NF^{X}_{MWP}$, and the second- and third-order spurious free dynamic range $SFDR^{X}_{2,MWP}$ and $SFDR^{X}_{3,MWP}$, are obtained from the optical spectral coefficients given by Eq.

(5)-(8). The input current to the RF part $x(t)$ is subject to the action of the nonlinear RF amplifier modeled by a transfer curve $y(t) = ax(t) + bx^2(t)$, where $a$ represents the amplifier gain and $b$ its second-order nonlinear coefficient. The currents at the input of the RF filter for the signal, second- and significant third-order distortion terms are then given by:

$$y_{\Omega_{1,2}}(t) = ai_1 \sin(\Omega_1 t + \theta_1) + b\{i_1 i_{11} \cos(\Omega_1 t + \theta_{11} - \theta_1) - i_2 i_{12} \cos(\Omega_1 t + \theta_2 + \theta_{12}) + i_2 i_{21} \cos(\Omega_1 t + \theta_2 - \theta_{21}) + i_2 i_{xx} \cos(\Omega_1 t + \theta_{xx} - \theta_2)\}; \quad (9)$$

$$y_{\Omega_1 - \Omega_2}(t) = ai_{12} \sin\left[(\Omega_1 - \Omega_2)t + \theta_{12}\right] + b\left\{i_1 i_2 \cos\left[(\Omega_1 - \Omega_2)t + \theta_1 - \theta_2\right] + i_{11} i_{xx} \cos\left[(\Omega_1 - \Omega_2)t + \theta_{11} - \theta_{xx}\right]\right\}; \quad (10)$$

$$y_{\Omega_2 - \Omega_1}(t) = ai_{21} \sin\left[(\Omega_2 - \Omega_1)t + \theta_{21}\right] + bi_{22} i_{xx} \cos\left[(\Omega_2 - \Omega_1)t + \theta_{22} - \theta_{xx}\right]; \quad (11)$$

$$y_{2\Omega_1}(t) = ai_{11} \sin(2\Omega_1 t + \theta_{11}) + b\left\{-\frac{i_1^2}{2}\cos(2\Omega_1 t + 2\theta_1) - i_{12} i_{xx} \cos(2\Omega_1 t + \theta_{12} + \theta_{xx}) + i_{21} i_{xx} \cos(2\Omega_1 t + \theta_{xx} - \theta_{21})\right\}; \quad (12)$$

$$\begin{aligned} y_{2\Omega_1 - \Omega_2}(t) &= ai_{112} \sin\left[(2\Omega_1 - \Omega_2)t + \theta_{112}\right] + b\left\{-i_1 i_{12} \cos\left[(2\Omega_1 - \Omega_2)t + \theta_1 + \theta_{12}\right]\right. \\ &\left. + i_1 i_{21} \cos\left[(2\Omega_1 - \Omega_2)t + \theta_1 - \theta_{21}\right] + i_2 i_{11} \cos\left[(2\Omega_1 - \Omega_2)t + \theta_{11} - \theta_2\right]\right\}. \end{aligned} \quad (13)$$

From Eqs. (9)-(13) one can get the overall processor FOMs as a function of the FOMs of the MWP part, the RF part gain $G_{RF} = a^2 |H_e(\Omega)|^2$, the RF Noise Figure $NF_{RF}$ and the RF amplifier parameters. This way, the processor Gain in logarithmic units is given by

$$G^X(dB) = G_{RF}(dB) + G^X_{MWP}(dB), \quad (14)$$

the processor Noise Figure by

$$NF^X(dB) = NF_{RF}(dB) + NF^X_{MWP}(dB), \quad (15)$$

while the processor second- and third-order SFDR are, respectively, given by

$$\begin{aligned} SFDR_2^X\left(dB{\cdot}Hz^{1/2}\right) &= SFDR^X_{2,MWP}(dB{\cdot}Hz^{1/2}) - \left[\left|H_{eN}\left(\Omega_1 - \Omega_2\right)\right|(\mathrm{dB}) + \frac{1}{2}NF_{RF}(\mathrm{dB})\right] - 5\log\left(1 + T_{2X}\right) \\ \text{for } T_2^X &= k\left(\frac{b}{a}\right)^2 \frac{\left|A^X_{\Omega_1}\right|^2 \left|A^X_{\Omega_2}\right|^2}{\left|A^X_{\Omega_1 - \Omega_2}\right|^2} = \frac{P_{IMD_2,RF}}{P_{IMD_2,MWP}} \\ \text{and } k &= \begin{cases} 4I_{dc}^2 \sin^4(\phi_{dc}) & \text{if } X = I, I - BD \\ 16I_{dc}^2 & \text{if } X = \Phi, \Phi - BD \end{cases}; \end{aligned} \quad (16)$$

$$\begin{aligned} SFDR_3^X\left(dB{\cdot}Hz^{2/3}\right) &= SFDR^X_{3,MWP}\left(dB{\cdot}Hz^{2/3}\right) - \frac{2}{3}\left[\left|H_{eN}\left(2\Omega_1 - \Omega_2\right)\right|(\mathrm{dB}) + NF_{RF}(\mathrm{dB})\right] - \frac{10}{3}\log\left(1 + T_{3X}\right) \\ \text{for } T_3^X &= k\left(\frac{b}{a}\right)^2 \frac{\left[\left|A^X_{\Omega_1}\right|^2 \left|A^X_{\Omega_1 - \Omega_2}\right|^2 + \left|A^X_{\Omega_1}\right|^2 \left|A^X_{\Omega_2 - \Omega_1}\right|^2 + \left|A^X_{2\Omega_1}\right|^2 \left|A^X_{\Omega_2}\right|^2\right]}{\left|A^X_{2\Omega_1 - \Omega_2}\right|^2} = \frac{P_{IMD_3,RF}}{P_{IMD_3,MWP}} \\ \text{and } k &= \begin{cases} 4I_{dc}^2 & \text{if } X = I, I - BD \\ 16I_{dc}^2 & \text{if } X = \Phi, \Phi - BD \end{cases}, \end{aligned} \quad (17)$$

where $|H_{eN}(\eta\Omega_1 - \Omega_2)|$ (dB) = $|H_e(\eta\Omega_1 - \Omega_2)|$ (dB) - $|H_e(\Omega_1)|$ (dB), for $\eta = \{1,2\}$, is defined as the normalized RF filter transfer function. The coefficients $T_2^X$ and $T_3^X$ represent the quotient between the RF power of the intermodulation distortion terms caused by the RF part, respectively $P_{IMD_2,RF}$ and $P_{IMD_3,RF}$, and the RF power of the intermodulation terms caused by the MWP part and subsequently amplified by the RF stage, respectively $P_{IMD_2,MWP}$ and $P_{IMD_3,MWP}$. This way, the greater the $T_2^X$ or $T_3^X$, the more limiting the effect of the distortion introduced by the RF part is to the dynamic range of the software-defined processor.

The behavior of the overall processor gain and noise figure predicted by Eqs. (14) and (15) is quite straightforward to interpret. The gain $G^X$ is actually the sum in logarithmic units of the MWP and RF part individual gains, hence the two parts can be designed independently to achieve an overall gain target. A similar behavior is observed for the overall noise figure $NF^X$ with respect to the noise figure values of the MWP and the RF parts. The situation is, however, different when we consider the dynamic range parameters since it is not possible, in principle, to decompose the contributions of the MWP and the RF parts as they are coupled by the $T_2^X$ and $T_3^X$ coefficients, Eqs. (16) and (17). As a consequence we focus our performance analysis on the evaluation of the spurious free dynamic range.

## 4. Application examples

An important advantage of the developed model is that it provides the overall FOMs for the software-defined MWP reconfigurable processor in terms of those corresponding to the MWP and the RF separate parts. Hence, it can be employed to evaluate the overall processor performance as well as the improvement or impairment that changes applied in either the MWP or the RF stages due to software reconfiguration will have on the global FOMs. This is especially useful in complex photonic circuit configurations, as the ones envisaged in the proposed versatile and application-agnostic MWP processor. In this section we apply our model to a set of application examples already reported in the literature so that we cover different optical filtering subsystems and detection schemes. We consider in particular: (1) an integrated frequency discriminator for phase-modulated microwave photonics links with direct balanced detection (FM-DD) [28]; (2) an integrated optical bandpass filter (BPF) with single detection [29]; and (3) an asymmetric Mach-Zehnder interferometer (MZI) with balanced detection [27,30]. Figure 4 illustrates the schematic layout of the three optical filters.

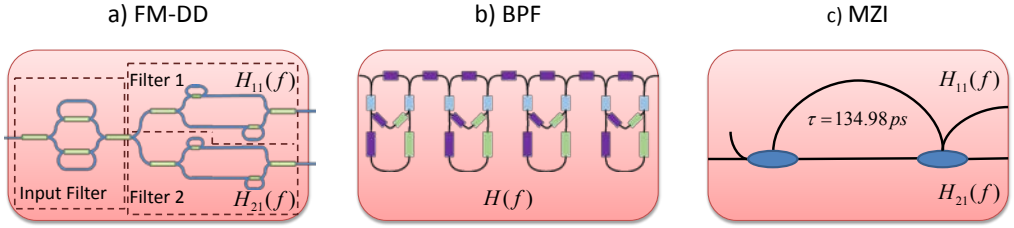


Fig. 4. Schematic top view of the three optical filtering subsystems considered: a) FM-DD, b) BPF and c) MZI

The closed-form expressions for the global FOMs derived in Section 3 [Eqs. (14)-(17)] require the knowledge of the two parallel optical transfer functions, $H_{11}(\omega)$ and $H_{21}(\omega)$, that describe the reconfigurable optical filtering subsystem for a given state of the configuration vector **C**. Figure 5 shows the transfer function of the three optical filter examples as a function of the microwave frequency $f = \Omega/2\pi$. We must note that the FM-DD operates in phase modulation, the BPF in intensity modulation, while we consider both intensity and phase modulation for the MZI. In all the scenarios we assume a monochromatic optical source whose spectral density function is approximated by a delta function. The following parameters are kept fixed in all the computations: Mach-Zehnder intensity modulator biased at quadrature point $\phi_{dc} = \pi/2$, $I_{dc} = 5$ mA, input and output resistances $R_{in} = R_{out} = 50\ \Omega$ and 20-dB RF amplifier gain ($a = 10$).

As it is shown in Fig. 4a, the PIC implementing the FM-DD is composed of two branches that are labeled as Filter 1 and Filter 2 and characterized, respectively, by $H_{11}(\omega)$ and $H_{21}(\omega)$. This photonic discriminator implements two functionalities: (1) the conversion of phase-modulated signals to intensity modulation and (2) the enhancement of the radio-over-fiber link performance by increasing the linearity and/or suppressing the noise. We consider two different frequency locations for the modulating tones: ($f_1 = 7$ GHz and $f_2 = f_1 + 1$ MHz) and ($f_1 = 5$ GHz and $f_2 = f_1 + 1$ MHz).

The integrated BPF is composed of four cascaded stages, each one implemented with ring resonators in an asymmetrical MZI structure with feedback [29], as depicted in Fig. 4b. By designing each filter stage to provide a pole, we obtain a bandpass response with a free spectral range of 15.6 GHz. In this case we place the microwave frequencies in the vicinity of the first resonance: $f_1$ = 16.5 GHz and $f_2$ = 14.7 GHz.

The asymmetric MZI is represented by the following two equivalent parallel optical filters:

$$H_{11}(\omega) = j\sqrt{\alpha_{MZI}}\, e^{j\omega\tau/2} \sin(\omega\tau/2) \quad \text{and} \quad H_{21}(\omega) = j\sqrt{\alpha_{MZI}}\, e^{j\omega\tau/2} \cos(\omega\tau/2) \tag{18}$$

where $\alpha_{MZI}$ = 1 is the MZI insertion loss and $\tau$ = 134.98 ps is the MZI differential time delay, [27,30]. We set the MZI to operate at quadrature, i.e. applying $\omega_0\tau = \pi/2$, and place the microwave tones at the frequencies $f_1$ = 17.3 GHz and $f_2$ = 15.3 GHz.

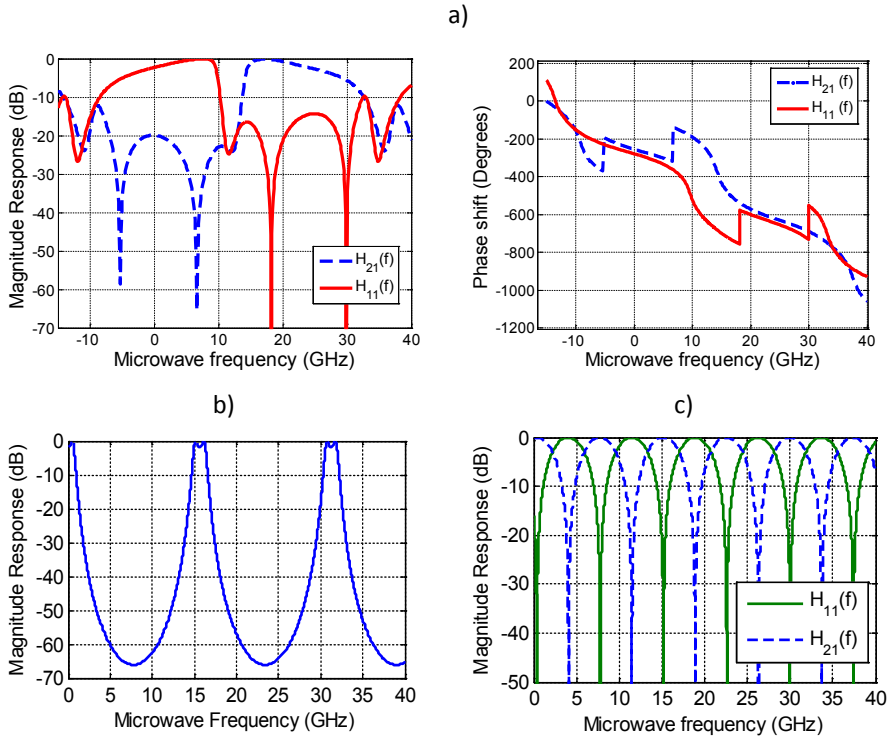


Fig. 5. Transfer function of the three optical filtering subsystems considered in function of the microwave frequency *f*: a) FM-DD (up), b) BPF (bottom left) and c) MZI (bottom right)

We stated in Section 3 that we cannot obtain the end-to-end processor dynamic range as the direct decomposition into its MWP and RF individual contributions. As concluded from Eqs. (16) and (17), the difference in the SFDR between the overall processor and the MWP stage, i.e. $SFDR^X_2$ - $SFDR^X_{2,MWP}$ and $SFDR^X_3$ - $SFDR^X_{3,MWP}$, depends on the $NF_{RF,}$ the normalized electrical filter response and the spectral coefficients $T_2{}^X$ and $T_3{}^X$.

Table I gathers the overall values of the processor FOMs computed for each one of the MWP application examples described above for a given RF stage. In particular, we consider a quasi-linear RF amplifier given by $b/a$ = 0.15 and $NF_{RF}$ = 4 dB and an electrical filter characterized by $|H_{eN}(\Omega_1)| = |H_{eN}(\Omega_2)|$ = 0 dB, $|H_{eN}(\Omega_1 - \Omega_2)|$ = -3 dB and $|H_{eN}(2\Omega_1 - \Omega_2)|$ = -2 dB. For this set of typical RF parameters, we find that the coefficients $T_2{}^X$ and $T_3{}^X$ are both << 1 since the quotient of the spectral optical coefficients $A^X_{\Omega_1}$, $A^X_{\Omega_2}$, $A^X_{\Omega_1-\Omega_2}$, $A^X_{\Omega_2-\Omega_1}$, $A^X_{2\Omega_1}$, $A^X_{2\Omega_2}$ and $A^X_{2\Omega_1-\Omega_2}$ in Eqs. (16) and (17) is not big enough as compared to the term $k(b/a)^2$, (which is of the order of $10^{-6}$ and $10^{-5}$ respectively for phase and intensity modulation). This means that for this particular design the impact of the MWP and the RF parts on the final dynamic range is

decoupled and fully decomposed, similarly to the behavior of the overall link gain Eq. (14) and noise figure Eq. (15). Under this condition, if we keep using a linear or quasi-linear RF amplifier ($b/a = 0.15$), the variation in the dynamic range, $SFDR^X_2$ - $SFDR^X_{2,MWP}$ and $SFDR^X_3$ - $SFDR^X_{3,MWP}$, will depend solely on the noise figure of the RF stage and the response of the electrical filter, [see Eqs. (16) and (17)]. In a first set of simulations we will analyze the impact of the RF part on the dynamic range when varying either $NF_{RF}$ or the absolute value of $H_{eN}(\eta\Omega_1 - \Omega_2)$.

**Table 1. Overall FOM computed values for the three optical filtering subsystems considered**

| Optical filter | Scheme *X* | $SFDR^X_2$ (dB·Hz$^{1/2}$) | $SFDR^X_3$ (dB·Hz$^{2/3}$) | $G^X$ (dB) | $NF^X$ (dB) |
|---|---|---|---|---|---|
| FM-DD ($f_1$ = 7 GHz) | Φ-*BD* | 99.68 | 105.36 | 0.17 | $NF^X_{MWP}$ (dB) + 4 |
| FM-DD ($f_1$ = 5 GHz) | Φ-*BD* | 88.02 | 102.27 | -3.60 | $NF^X_{MWP}$ (dB) + 4 |
| BPF | *I* | 84.36 | 115.71 | -7.87 | $NF^X_{MWP}$ (dB) + 4 |
| MZI | *I-BD* | 83.11 | 107.54 | -5.20 | $NF^X_{MWP}$ (dB) + 4 |
| | Φ-*BD* | 79.79 | 109.28 | 1.75 | $NF^X_{MWP}$ (dB) + 4 |

Figure 6 (left) shows both the second- and third-order distortion variations as a function of $NF_{RF}$ for all the optical filtering subsystems considered. As described before, the results are identical for all the MWP stage cases evaluated since $T_2^X$ and $T_3^X$ are negligible. The difference in the slopes for the SFDR variation can be understood from Eqs. (16) and (17) since this variation has a slope of -1/2 for second-order nonlinearities while -3/2 for third-order nonlinearities. We can see that for a 3-dB degradation of the SFDR variation this behavior results in a maximum $NF_{RF}$ change of 6.2 and 4.5 dB, respectively. Figure 6 (right) illustrates the impact of the magnitude value of the RF filter at the frequencies of the intermodulation terms when keeping the rest of the simulation parameters fixed. Again, identical performance results were obtained for each one of the designs of the MWP stage. We can see how the SFDR variation increases as the absolute value of $H_{eN}(\eta\Omega_1 - \Omega_2)$ decreases. The different slopes for the SFDR variation are also understood from Eqs. (16) and (17) since this variation has a logarithmic slope of -1 and -2/3, respectively, for the second- and third-order nonlinearities. We can see that the dynamic range related to the MWP part can be improved (SFDR variation greater than 0 dB) if the undesired distortion term is sufficiently rejected by the RF filter. To be more precisely, $SFDR^X_{2,MWP}$ and $SFDR^X_{3,MWP}$ are unaltered (SFDR variation of 0 dB) respectively for a 4-dB and 8-dB rejection of the RF distorting term as compared to the RF signal tone. This information is actually very useful since it allows to properly design the RF filtering stage in order to improve the dynamic range of the MWP subsystem.

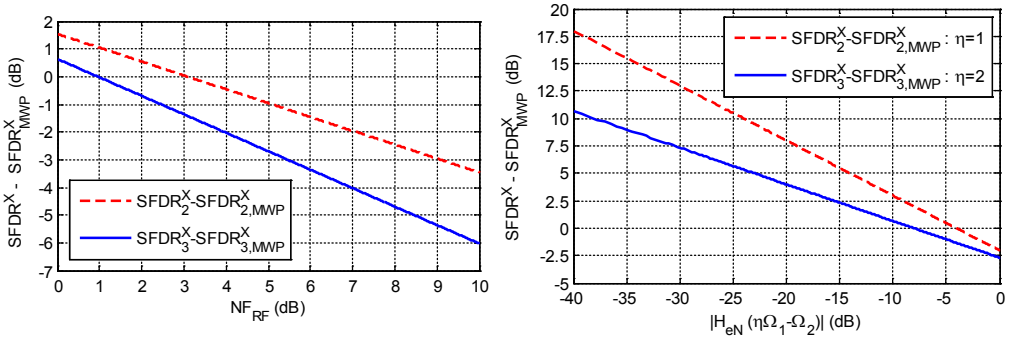


Fig. 6. SFDR variation as a function of $NF_{RF}$ (left) and as a function of $|H_{eN}(\eta\Omega_1 - \Omega_2)|$, $\eta = \{1,2\}$, (right), for all the optical filtering subsystems considered: FM-DD, BPF and MZI

In a second set of simulations, we analyze the impact of the RF amplifier linearity on the SFDR variation as a function of the ratio $b/a$ in the range [0,10] when keeping fixed $NF_{RF}$ and $H_{eN}(\eta\Omega_1 - \Omega_2)$. Note that $b/a$ relationships for commercial RF amplifiers are often in the range [0.1-2], but it is extended to 10 to incorporate the most nonlinear cases. Under this parametrization condition, the dynamic range variation behaves differently when we compare the different optical filtering subsystems considered. For the BPF and the MZI examples, the impact of the RF amplifier linearity is not significant and we obtain nearly constant values for both dynamic range variations: $SFDR^X_2 - SFDR^X_{2,MWP} = -0.45$ dB and $SFDR^X_3 - SFDR^X_{3,MWP} = -2.02$ dB. However, a different behavior is observed in the case of the optical frequency discriminator depending on the location of the modulating tones. Figure 7 shows the SFDR variation as a function of the ratio $b/a$ for the FM-DD for both modulating conditions and different values of the RF noise figure. On one hand, we see in Fig. 7 (up) how the variation of the second-order SFDR for the microwave frequencies $f_1 = 7$ GHz and $f_2 = f_1 + 1$ MHz (solid lines) decreases substantially as the non-linearity of the RF amplifier increases. This is sustained by the fact that the impact of the MWP and the RF parts on the overall dynamic range is coupled by the spectral term $T_2^X$. The 3-dB degradation point at $b/a = 2.65$ sets the boundary between the MWP-limited and the RF-limited second-order SFDR. On the other hand, the SFDR variation becomes nearly constant if the microwave tones are placed at the frequencies $f_1 = 5$ GHz and $f_2 = f_1 + 1$ MHz (dashed lines) since, in this case, the spectral coefficients given by Eqs. (5)-(8) reduce the $T_2^X$ contribution. A similar condition is indeed shown in Fig. 7 (down) for the third-order SFDR where the dynamic range variation remains constant with the ratio $b/a$ for both modulating conditions.

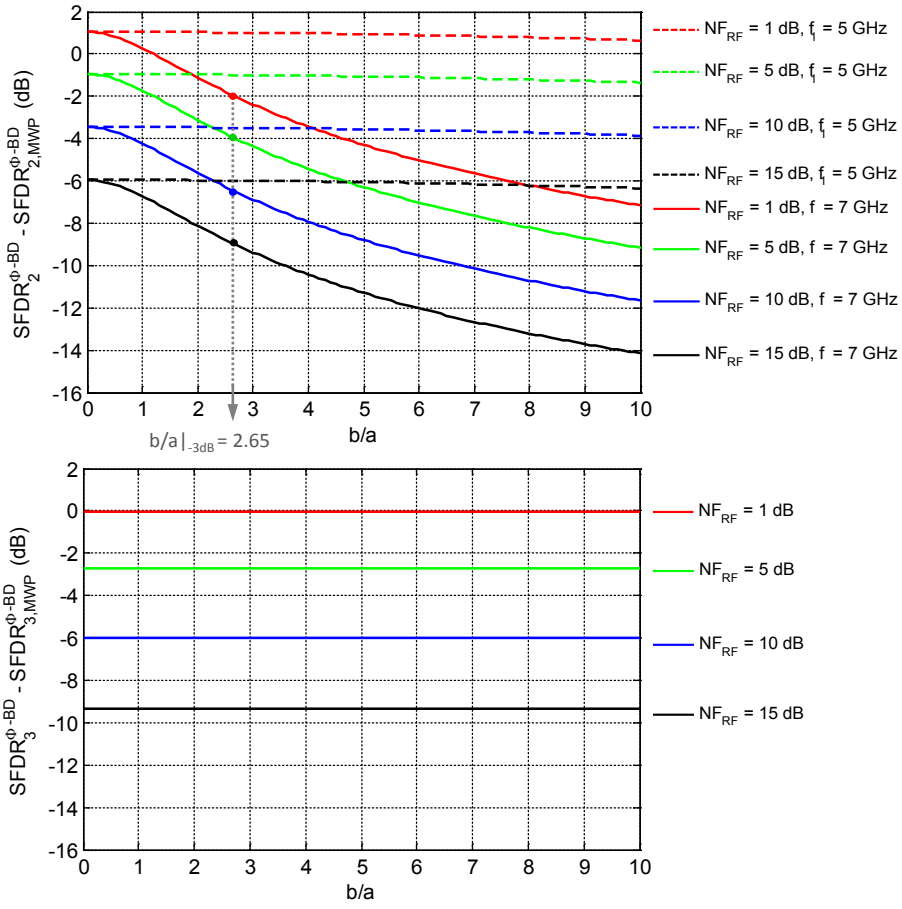


Fig. 7. Second- (up) and third-order (down) SFDR variation as a function of $b/a$ for the FM-DD

## 5. Discussion

The model developed in Section 3, condensed in Eqs. (14)-(17) and exemplified in Section 4, is extremely powerful and comprehensive. It provides analytical expressions for the evaluation of the main figures of merit characterizing the full end-to-end performance of the processor and taking into consideration the impact of both the photonic and the RF parts. Although these figures are expressed in terms of internal parameters and transfer functions that can be changed by means of suitable programming, the overall expressions are common for all the represented cases, regardless of the particular functionality for which the processor is programmed at a given instant of time.

In addition, the model provides a simple physical interpretation of the roles played by the photonic and the RF parts, even in the case of nonlinear operation. As far as gain and noise figures are concerned, Eqs. (14) and (15) predict an uncoupled and additive behavior (in dB units) of the photonic and RF parts. Therefore, if the impact of nonlinearity is of no particular concern the designs of both parts can be carried independently. The processor performance as far as dynamic range is concerned, which is described by Eqs. (16) and (17) for second- and third-order nonlinearities respectively, shows a coupled behavior between the two stages. For instance, considering third-order nonlinearities (a similar analysis can be carried out with second-order nonlinearities) the overall SFDR in Eq. (17) is composed of three terms. The first one corresponds to the dynamic range related to the photonic stage, $SFDR^{X}_{3,MWP}$ (dB·Hz$^{2/3}$), and is shown in Fig. 8.

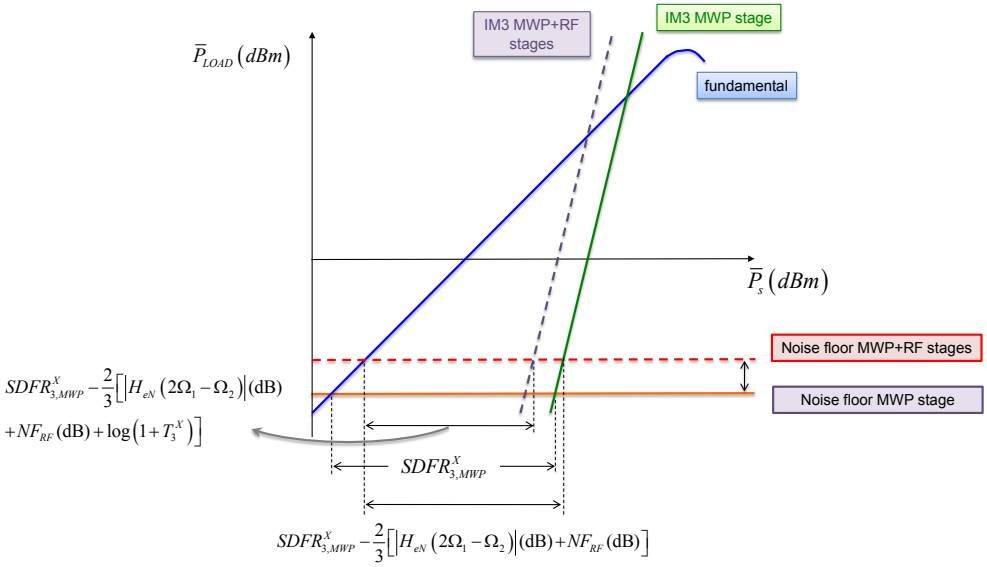


Fig. 8. Impact of the three terms in Eq. (17) on the overall third-order SFDR of the processor.

The second term is an uncoupled contribution arising from to the RF stage that can improve or degrade the dynamic range of the preceding photonic part. The first case happens when the undesired nonlinear term is sufficiently rejected by the RF filter so that $|H_{eN}(2\Omega_1 - \Omega_2)|$ (dB) + $NF_{RF}$ (dB) < 0. In the second case, $|H_{eN}(2\Omega_1 - \Omega_2)|$ (dB) + $NF_{RF}$ (dB) > 0, the dynamic range is degraded as it is shown in Fig. 8. The third term represents the coupling between the photonic and the RF sections of the processor. This coupling depends on the parameter $T_3^X = P_{IMD3,RF} / P_{IMD3,MWP}$ that relates the RF power of the nonlinear terms generated at the RF and the photonic parts of the processor. The coupling appears because part of the nonlinearities generated by the RF stage are due to the mixing of nonlinear terms generated by the previous photonic stage. Its effect is the shifting of the system's $IMD_3$ curve as shown in Fig. 8. In fact, if the nonlinear coefficient $b$ of the RF part vanishes, then $T_3^X = 0$ and the third

term in Eq. (17) becomes zero and therefore both the photonic and RF parts can be independently designed as far as RF gain, noise figure and dynamic range parameters are concerned.

It is expected that NF and SFDR tradeoff relationships when designing the general processor architecture will be substantially different than those of ASPICs. This is due to the fact that the former will most probably include generic optical amplifying stages that will increase the noise floor and switching loopbacks, which will increase losses. However, at the same time, the filtering stages will have the possibility of reconfiguration and thus provide a higher suppression of intermodulation terms. All in all, the processor architecture is expected to provide different programming alternatives towards obtaining more flexible NF and SFDR tradeoff relationships.

Depending on the required functionality, either an overall linear operation will be targeted (e.g. microwave filtering, beam-steering, etc.), whereas in other cases, it is the nonlinear performance that needs to be boosted (e.g. up- and down-conversion, frequency multiplication, etc.). The model presented here will provide a valuable tool for the design of both the photonic and RF stages and, if required, the necessary coupling between them to exacerbate an overall nonlinear behavior.

## 6. Conclusions

We have proposed a software-defined reconfigurable MWP signal processor architecture that can be integrated on a chip and is capable of performing all the main functionalities by suitable programming of its control signals. A potential application of this software-defined processor lies in the design of programmable and tunable multiband RF front-ends required for the future 5G telecommunication networks [31]. A thorough end-to-end design model has been derived that accounts for the performance of the overall processor taking into consideration the impact of both its photonic and RF parts and showing as well their interdependencies. The model has been employed to characterize several application examples in order to show its versatile nature. As far as the overall RF gain and Noise Figure are concerned, the photonic and RF sections are decoupled and thus their designs can be carried out independently. Regarding the overall dynamic range, the photonic and RF sections are coupled since part of the nonlinearities generated by the later are due to the mixing of nonlinear terms generated by the former. However, if the nonlinear coefficient $b$ of the amplification stage in the RF part vanishes, then the photonic and RF parts can be independently designed as well. Depending on the required MWP functionality, the processor can be programmed to feature an overall linear behavior or to boost the generation of a given nonlinear term. The model developed and presented here provides a powerful tool to design and evaluate the required values of the relevant performance parameters, which would then need to be programmed to run on the multi-purpose chip architecture. It is important to point out that for the proposed processor the RF and photonic parts should be integrated into a single chip. In the current state of the art this photonics/ RF electronics integration has not been completely developed yet. Furthermore, this might require a hybrid approach bringing together two different material platforms. This being stated, there are ongoing efforts to achieve this target on a medium-term: For instance, the recently published 2015 roadmap for the JEPPIX platform [32] targets the first InP and BiCMOS electronics demonstrators by 2018 and combined wafer scale photonic-electronic integration in 2020.

## Acknowledgments

The authors wish to acknowledge the financial support given by the Research Excellency Award Program GVA PROMETEO II/2013/012 and the FPI-UPV Ayudas de Investigación y Desarrollo (PAID) Program from the Universitat Politècnica de València.